Thrombus Detection in CT Brain Scans using a Convolutional Neural Network

Aneta Lisowska[1,2], Erin Beveridge[1], Keith Muir[3] and Ian Poole[1]
[1]*Toshiba Medical Visualization Systems Europe Ltd., 2 Anderson Place, Edinburgh, U.K.*
[2]*School of Engineering and Physical Sciences, Heriot-Watt University, Edinburgh, U.K.*
[3]*Queen Elizabeth University Hospital, University of Glasgow, Glasgow, U.K.*

Keywords: Convolutional Neural Network, Stroke, Thrombus, Non-contrast Computer Tomography (NCCT).

Abstract: Automatic detection and measurement of thrombi may expedite clinical workflow in the treatment planning stage. Nevertheless it is a challenging task on non-contrast computed tomography due to the subtlety of the pathological intensity changes, which are further confounded by the appearance of vascular calcification (common in ageing brains). In this paper we propose a 3D Convolutional Neural Network architecture to detect these subtle signs of stroke. The architecture is designed to exploit contralateral features and anatomical atlas information. We use 122 CT volumes equally split into training and testing to validate our method, achieving a ROC AUC of 0.996 and a Precision-Recall AUC of 0.563 in a voxel-level evaluation. The results are not yet at a level for routine clinical use, but they are encouraging.

1 INTRODUCTION

Detection of subtly discriminated regions in volumetric medical imaging is challenging. An example is the detection of stroke signs in non-contrast computed tomography (NCCT), where thrombi are one of the pathologies of interest. Thrombi manifest as subtle vascular intensity and texture changes which are challenging to identify due to the proximity of bone, and the similarity to normal age related vascular calcification (see Figure 1).

Automatic detection of thrombi and their subsequent measurements may provide information which is important for treatment planning. For example, the length of the thrombus observed in thin slice NCCT is related to the success rate of thrombolysis, a treatment aimed to recanalise occluded arteries (Riedel et al., 2011). Nevertheless, to our knowledge, the problem of automatic thrombus detection has not been directly addressed.

Detection of stroke signs in CT scans has previously been demonstrated at the *brain* level. Chawla *et al*. proposed a general system for classification of ischaemic and haemorrhagic stroke signs (Chawla et al., 2009). Their system computes a separate histogram of intensity values for each hemisphere, and the classification of the image slice is based on the comparison between the left and right histograms. The authors report good performance in determining the type of stroke, but the system is not designed to give a precise location of the stoke sign. Furthermore the haemorrhage is easily detectable on CT compared to ischaemia or thrombus.

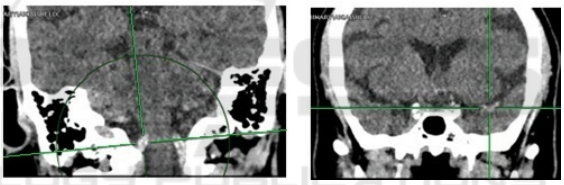

Figure 1: Left: Normal calcification of arteries, which could be confused with abnormal dense vessel signs. Right: Example of a CT brain scan with a clearly visible dense vessel.

Precise location of stroke signs requires a more localised model. One approach is to compare the patient image with a normative atlas created from healthy examples of anatomy; the patient image is registered to the normative atlas and the pathology is identified by the differences between the reference atlas and the examined image (Doyle et al., 2013). This approach requires accurate non-rigid registration, which may not always be possible due to anatomical variability. Machine learning algorithms are one method of learning diverse non-parametric appearance models. For instance, random forest classifiers have been successfully applied to various medical imaging segmentation tasks (Geremia et al., 2011; Zikic et al., 2012). However, in recent years CNN-based solutions have dominated brain image analysis applications, resulting in the best performance in the Ischemic Stroke Le-

Lisowska A., Beveridge E., Muir K. and Poole I.
Thrombus Detection in CT Brain Scans using a Convolutional Neural Network.
DOI: 10.5220/0006114600240033
In *Proceedings of the 10th International Joint Conference on Biomedical Engineering Systems and Technologies (BIOSTEC 2017)*, pages 24-33
ISBN: 978-989-758-215-8

sion Segmentation (ISLES) (winning solution in 2015 (Kamnitsas et al., 2016)) and Brain Tumor Segmentation (BRATS) challenges (see CNN based application (Havaei et al., 2016) (Pereira et al., 2015)). These CNN solutions are trained on brain MRI data, however CNNs have also been applied to CT images of the knee (Prasoon et al., 2013) and lungs (Anthimopoulos et al., 2016). The CNN architecture design may differ between the imaging modalities and between various anatomies of interest. (Li et al., 2014) observe that CT images lack structural detail in regions of soft tissue, taking on a textured appearance, therefore there are few higher-level concepts for a deep network to learn. Prasoon *et al.* also avoided use of deep architecture in CT and pointed out that thin structure of cartilage can be lost if too many mean-pooling layers are applied (Prasoon et al., 2013). In this paper we employ a fully convolutional architecture, which is only 7 layers deep as described in Section 2.

CT scans are three-dimensional (3D), and therefore architectures designed for images cannot be directly applied. When moving to 3D data, three strategies are common. Firstly, the volume may be treated as a stack of 2D slices on which a 2D architecture is directly applied. Volumes are often acquired in a slice-wise manner, and where the slice spacing is large, this may be a natural approach. The second strategy is a *triplanar* CNN (Prasoon et al., 2013; Yang et al., 2015) in which axial, sagittal and coronal slices centred at the voxel of interest are considered separately and fed to three 2D CNNs (or three channels of a 2D CNN (Roth et al., 2014; Wolterink et al., 2015)). Their outputs are combined in the preclassification stage. Finally, 3D convolution (Urban et al., 2014; Kamnitsas et al., 2015; Payan and Montana, 2015) may be used in place of 2D convolution. This last strategy is computationally expensive, thus training and optimisation of a network can be arduous. Payan and Montana compared a 2D CNN with a 3D CNN on brain MRI data and found that the 3D CNN obtained marginally better Alzheimer classification accuracy (Payan and Montana, 2015). In this paper we adopt a 3D CNN, but we apply spatial decomposition of the kernels to address the computational complexity issue such that convolutions are applied one dimension at the time.

A key element of our architecture is bilateral feature comparison. The idea of bilateral feature comparison is strongly linked with exploitation of anatomical symmetry, which has been also incorporated in unsupervised approaches of pathology detection. Researchers utilised in-organ symmetry for detection of tumours in the brain (Hasan et al., 2016; Zhao et al., 2013) and prostate (Qiu et al., 2013). There have also been attempts to examine symmetry between a pair of organs in breast tumour detection (Erihov et al., 2015; Bandyopadhyay, 2010). In these approaches, the pathology is found by searching for the most dissimilar regions between the left and right side of the organ (Hasan et al., 2016), or by identification of asymmetry between paired organs (Erihov et al., 2015). It is rare that a stroke will occur in both sides of the brain in a given episode, therefore comparison between hemispheres helps to discriminate between subtle changes in the affected side and the normal brain tissue. We hypothesise that exploiting contralateral features will therefore be useful when detecting thrombi.

The second key element of our architecture is the explicit incorporation of spatial anatomical context by provision of the coordinates in a (rigidly-registered) reference dataset "atlas" by adding three channels encoding x, y, z atlas locations. In this, we follow the lead of authors such as (O'Neil et al., 2015) who used atlas coordinates as a feature provided to a random forest when learning to detect anatomical landmarks. The injection of contextual information into a machine learning algorithm was demonstrated in a traumatic brain injury application by (Rao et al., 2014) who used multi-atlas propagation and EM (MALPEM) (Ledig et al., 2012) to obtain tissue classes priors which were later exploited in a random forest. Since the thrombi may be subtle, the addition of anatomical context might provide a helpful insight.

One of the challenges in training a CNN to detect thrombus is the significantly limited set of samples containing pathology compared to healthy tissue. As a result, the CNN may take little account of the underrepresented class during training. One solution to address this problem is to alter the loss function. For neutrophil detection, (Wang et al., 2015) penalised more heavily the misclassification of non-neutrophils than that of neutrophils, by doubling the computed softmax loss. (Brosch et al., 2015) designed a specialised CNN objective function which relies on a weighted combination of sensitivity and specificity. A more mechanical approach is to take all samples from the underrepresented category and a random subset of the examples from the other category (Ciresan et al., 2012; Roth et al., 2014; Li et al., 2015; Rao et al., 2015). However, random sampling of classes may not always give the most useful training distribution. A number of papers deliberately biased the training distribution towards examples which were more difficult to classify due to visual proximity between classes. Researchers commonly sampled background more densely close to the region of interest compared to other areas (Ciresan et al., 2013; Prasoon et al., 2013; Dvorak and Menze, 2015). Re-

cently, (Kamnitsas et al., 2016) suggested that training on large image segments allows for automatic adjustment to this problem. In this paper we choose to use a weighting function to compensate for the unbalanced sample distribution such that normal and abnormal samples count equally in the loss function.

In summary, this paper makes three contributions:

- We propose a 3D CNN architecture incorporating brain symmetry exploitation and atlas information (Section 2). We present qualitative and quantitative results obtained by applying the proposed CNN to the thrombus detection problem (Section 4.2).
- As far as we are aware, this is the first CNN-based solution applied to brain NCCT and the first solution for automatic thrombus detection.
- We study the effect of the training procedure on efficiency. We compare patch and segment based training to full block training with and without weighting of the loss function in order to identify the most effective training strategy in an unbalanced sample setting (Section 4.1).

2 METHODS

We propose a convolutional neural network (CNN) which leverages left and right hemisphere comparison (See Figure 3). The first steps consist of isotropic resampling to 1mm voxels and alignment of the CT volumes to a reference dataset designated as an atlas. The transformation between a given dataset and a reference atlas is discovered via landmarks, which are detected in the novel volume by random forest as proposed in (Dabbah et al., 2014). A block of interest extending into the sagittal plane is then extracted and folded along the brain midline, similarly to the folding of a butterfly's wings (see Figure 2). This folding results in two 3D CNN intensity channels relating to the target and contralateral sides of the brain, enabling bilateral comparison. We call this architecture a Butterfly CNN. Since the architecture works in the folded space, it is left-right agnostic with respect to the target laterality. The target and contralateral channels may thus correspond to either left and right, or right and left, respectively. Consequently there is sharing of training data between left and right hemispheres.

Alongside the two data input channels, we insert three channels encoding the x, y and z atlas coordinates to the architecture. For the convolution operations, we use a spatial decomposition of a 5x5x5 filter e.g. three layers of orthogonal one-dimensional convolutions: 5x1x1, 1x5x1, 1x1x5. $N_I = 32$ kernels are used for the data channels and $N_A = 4$ kernels are used for the atlas channels. Channels are then merged and another convolution operation is applied, with $N_M = 32$ kernels. See Figure 3 for a diagram of the architecture. ReLU activation functions are used. The output is fully convolutional allowing for the efficient prediction of all voxels of the dataset in a single pass.

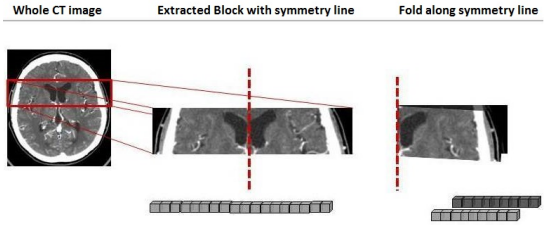

Figure 2: Block extraction.

The model was implemented in Python using the Keras library built on top of Theano. Training was performed using stochastic gradient descent on normalised data samples, with learning rate 0.001, optimising the squared *hinge loss* function, momentum 0.9 and L2 regularisation 0.002.

3 MATERIALS

We use data from the South Glasgow Stroke Imaging Database, which includes the following studies: ATTEST (Huang et al., 2015), POSH and WYETH (Wardlaw et al., 2013) provided by the Institute of Neuroscience and Psychology, University of Glasgow, Southern General Hospital. Ground truth was collected on the acute non-contrast CT (NCCT) scan for 122 patients with suspected acute ischaemic stroke within 6 hours of onset. Manual segmentations of thrombi were generated in 3D Slicer 4.5.0 by a clinical researcher under the supervision of an experienced neuroradiologist. Annotations were blind to additional scans (e.g. CT angiography, CT perfusion, follow-up scans) and clinical information with the exception of the laterality of the symptoms. Current methods are applied only to the anterior circulation but consider both proximal occlusions and more distal dot signs.

There might be some uncertainty around precise segmentation of the thrombi. Since we are interested only in detection, it is undesirable for the network to waste learning capacity trying to refine the boundary. We consider a border, 2mm in width around each abnormality, as a "do not care" zone. Such voxels do not influence the loss function which drives the stochastic gradient descent, nor are they included in the results.

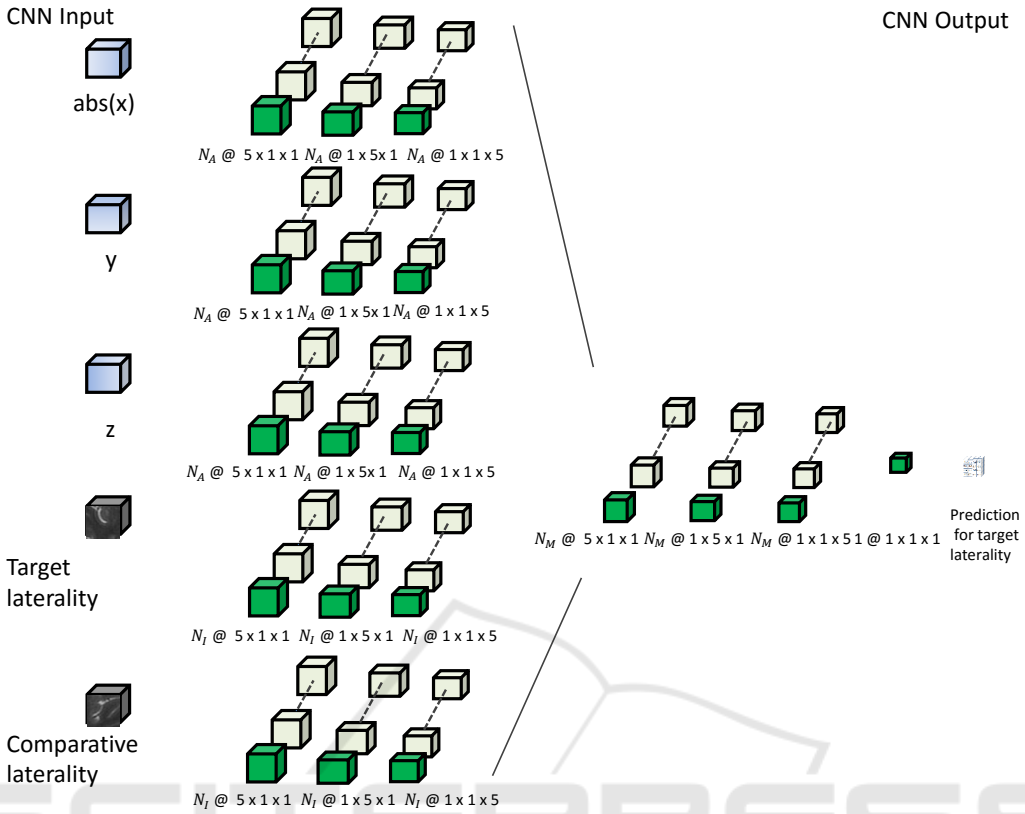

Figure 3: Schematic of the CNN architecture.

For implementation, we use -1 and +1 to represent normal and thrombi voxels respectively, and use the value 0 to represent the ”do not care” voxels. The border zone is constructed using morphological dilation.

For training and testing of the CNN classifier we used a Titan X GPU.

4 EXPERIMENTS

The data was split equally (and randomly) into 61 training datasets and 61 testing datasets.

We evaluated the performance of the CNN in Section 4.2 in terms of the area under the curve (AUC) for the Receiver Operating Curve (ROC AUC) and the precision-recall (PR AUC) curve. The ROC curve represents the relationship between sensitivity (i.e. recall) and specificity, while the PR curve represents the relationship between precision and recall. Sensitivity (recall) is a measure of how many of the positive samples have been correctly identified as being positive. Specificity is a measure of how many of the negative samples have been correctly identified as being negative. Precision is a measure of how many of the samples predicted by the classifier as positive are indeed positive. It is suggested that PR curves should be used when the positive class samples are rare compared to the negative class samples (Davis and Goadrich, 2006), because precision is more sensitive to any change in the number of false positives, while specificity is not due to the large number of negative samples. As an example, if the ratio of normal to abnormal is $10,000 : 1$ then even a false positive rate of 0.01 results in 100 false detections.

4.1 Patch vs. Full Block Training

In our efforts to establish the most efficient training procedure, we compare training of the CNN with whole blocks as input versus training with small patches as input. We introduce a weighting factor w to allow for the correction of the imbalance between normal and abnormal samples. We define w as the ratio of normal to abnormal voxels in the training set. The CNN architecture as presented in Figure 3 is used, but with smaller filter size 3x3x3 and trained only for 250 epochs. We are primarily interested in the training time of the network, but we also report PR AUC to ensure the learning took place.

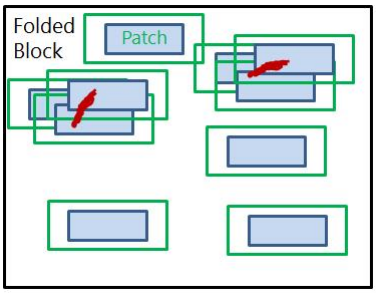

Figure 4: 2D representation of biased patch selection process. More patches of abnormality than normality are selected, in order to compensate for the presence of normal voxels within the abnormal patches, to achieve a balanced training set. The green box represents the field of view (a margin) and the blue box is the core patch size, for which predictions are being output during training.

For the patch training, we sample equal numbers of normal and abnormal locations, but we vary the size of the core patch that we extract at each location. The core size corresponds to the voxels for which the response is computed. In practice, we require a larger input patch to the network, in order to include a margin of voxels for which the filter response is not computed, as we employ *valid-mode* convolutional operations. In one dimension and input patch size P, convolving with filter F will produce a feature map M of size $P-F+1$. Therefore, to produce an output of 1 voxel after 2 convolutions with filter size 3 in each dimension, the input patch size is 5^3. The core patch size of 1 will have samples only from one class, nevertheless inputs with a larger core patch size are likely to have voxels from both classes when an abnormal patch is extracted (See Figure 4. This case resembles the image segment training procedure of (Kamnitsas et al., 2016). The results obtained for 3 different input patch sizes and full folded block training are presented in Table 1.

We found that full block training took significantly longer than patch-based training. It is evident that weighting of the loss function is necessary to compensate any severe imbalance of training data samples, as is the case when the CNN is trained on the full block or large patches. For the core patch size 1^3, no learning occurred when using either a weighted or an unweighted loss function. It might be due to exposure of the network to insufficient number of training voxels, which is not a problem when trained on the larger patches. The network trained on core patch size 1^3 might not have seen the difficult examples which are close to the lesion borders, which would always be included when training on the larger patches.

In a further experiment we train the CNN on large patches with a weighted loss function. This allows for efficient training without the need for extensive experimentation to select an appropriate patch size, for which weighting of the loss function is not required.

Table 1: The table shows the precision-recall AUC achieved on a test dataset after just 250 epochs of training and corresponding training time. PBT (Patch based training), FBT (Full Block Training), PBTw (Patch based training with loss function weighting), FBTw (Full Block Training with loss function weighting).

Method	Precision-Recall AUC	Training time
PBT (core patch 1)	0.015	1.50 h
PBTw (core patch 1)	0.023	1.52 h
PBT (core patch 5)	0.341	29.3 min
PBTw(core patch 5)	0.320	29.4 min
PBT (core patch 10)	0.006	36.4 min
PBTw (core patch 10)	0.347	36.2 min
FBT	0.002	16.7 h
FBTw	0.397	16.6 h

4.2 Thrombus Detection Results

The CNN detector (as presented in Figure 3) was trained for 800 epochs on input patches of size 24^3 (core patch 16^3) extracted from 61 training datasets. The detector was evaluated on 61 testing datasets and the quantitative results are presented in Table 2. Training took 2.15h and detection time/ per block is 4s.

For comparison we trained also a simple CNN network which is composed from 7 layers and the number of kernels and filter sizes are the same as in the Figure 3 the difference is that it has only one input channel. The bilateral comparison and atlas information is not incorporated in the simple CNN.

The precision-recall curves for both the simple and the Butterfly CNNs are shown in Figure 5 and the ROC for the Butterfly CNN is shown in Figure 6. Some example detection results are presented in Figure 7 and Figure 8. The former show a case of very subtle thrombus where we fail to detect it at the sagittal slice of the abnormality and quite a few false positives are visible in the maximum intensity projection (MIP) view. The latter is more clearly visible thrombus and the detections are almost perfect.

Table 2: Thrombus detection evaluation.

Model	ROC AUC	Precision-Recall AUC
Butterfly CNN	0.997	0.562
Simple CNN	0.996	0.178

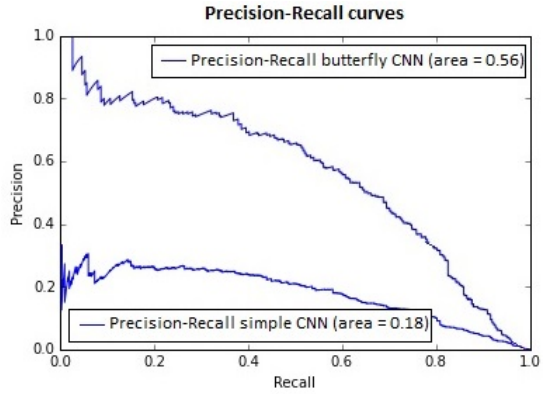

Figure 5: Precision-Recall curves for Simple CNN and Butterfly CNN. At the point that around 70% of thrombi are detected the simple CNN would give around 20% true detection results whereas the Butterfly CNN would produce just above 50% of true detection results.

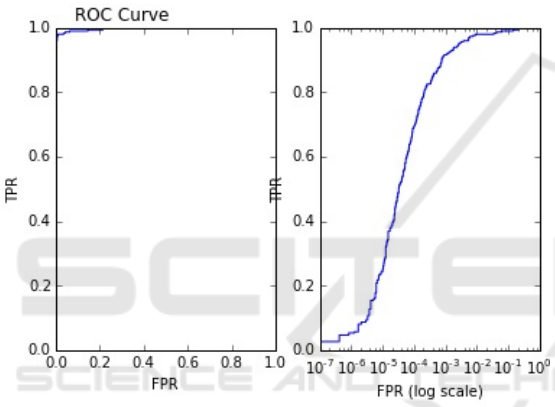

Figure 6: Left: ROC curve in full. Right: ROC curve shown with a log scale on the specificity axis, to focus on the range of interest. For the thrombus detector to be clinically useful the false positive rate at the voxel level needs to be very low, of order 10^{-4} or better, otherwise false positive detections will overwhelm true positives.

5 DISCUSSION

We have found that weighting of the loss function to compensate for unbalanced training data is effective, even essential, when training either on the full block or using a large image patches. Patch-based training is significantly faster than full block training. The downside of this approach is that it requires careful selection of the size of the patches when the weighting of the loss function is not applied. To overcome this difficulty we have adapted the combination of larger path and weighting of the loss function for training of the thrombus detector.

The quantitative and visual results obtained using presented solution are encouraging. However, to reach detection performance level at which the detector could be applied clinically the number of the false positive detections needs to be further reduced. To achieve this we will consider adapting a cascade approach similar to boosting, so that a second classifier is trained only on on normal examples which were misclassified at the first detection stage, this might help to eliminate false positive detections (Liswoska et al., 2016).

The proposed architecture for thrombus detection performs better than a single channel CNN. This supports our hypothesis that incorporation of atlas information and bilateral features within the CNN architecture is helpful when identifying subtle stroke signs. In future experiments it would be interesting to evaluate the extent to which each of the architectural choices contribute to the thrombus detection performance and whether the level at which they are inserted to the CNN architecture affects their usefulness.

Large amount of medical imaging data is difficult to obtain, especially given the requirement for ground truth labels provided by expert clinicians. Researchers have tried to address this problem by using transfer learning. In this scheme a network first trained on large annotated natural image datasets like ImageNet, followed by fine-tuning on the smaller medical imaging dataset. (Shin et al., 2016) found this approach to be beneficial when applied to both thoracoabdominal lymph node detection and interstitial lung disease classification in CT scans. On the other hand (Arevalo et al., 2015) and (Gao et al., 2016) found that CNN models trained fully with the domain images performed better than models pretrained on the ImageNet dataset when applied to the problems of mammography mass lesion classification and Interstitial Lung Disease Pattern Detection in CT respectively. It is unclear if this training approach would be helpful for thrombus detection; further investigation is required. An interesting avenue to explore might be knowledge transfer between two medical image datasets or alternatively between two different tasks.

We hypothesise that the proposed CNN architecture would also be well suited to the detection of other stoke signs and we plan to train it on ischaemic regions in future study. This will provide an opportunity to evaluate benefits coming from within-domain transfer learning. The model trained purely on ischaemic data can be compared to the thrombus detection model fine-tuned for ischaemia detection problems.

Future assessment of the detector performance will also include patient level evaluation and testing on more brain CT datasets from different institutions.

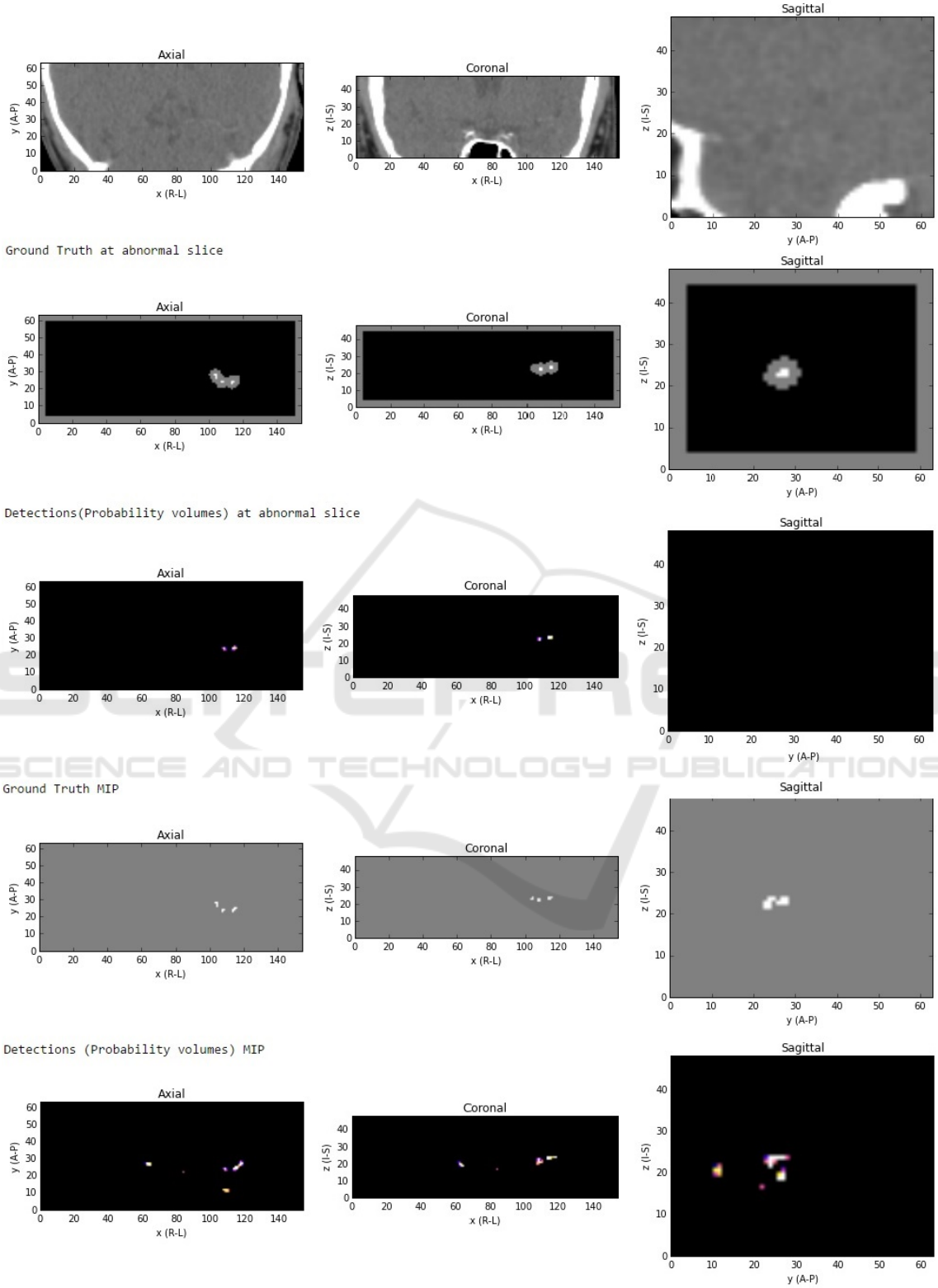

Figure 7: Top to bottom: CT image at the abnormal slice, ground truth segmentations at the abnormal slice (here: gray region is a ”do not care” zone), detection at the abnormal slice (note misdetection in a sagittal slice), ground truth in a projection view through the whole volume, detection in a projection through the volume (a few false positive detections are present).

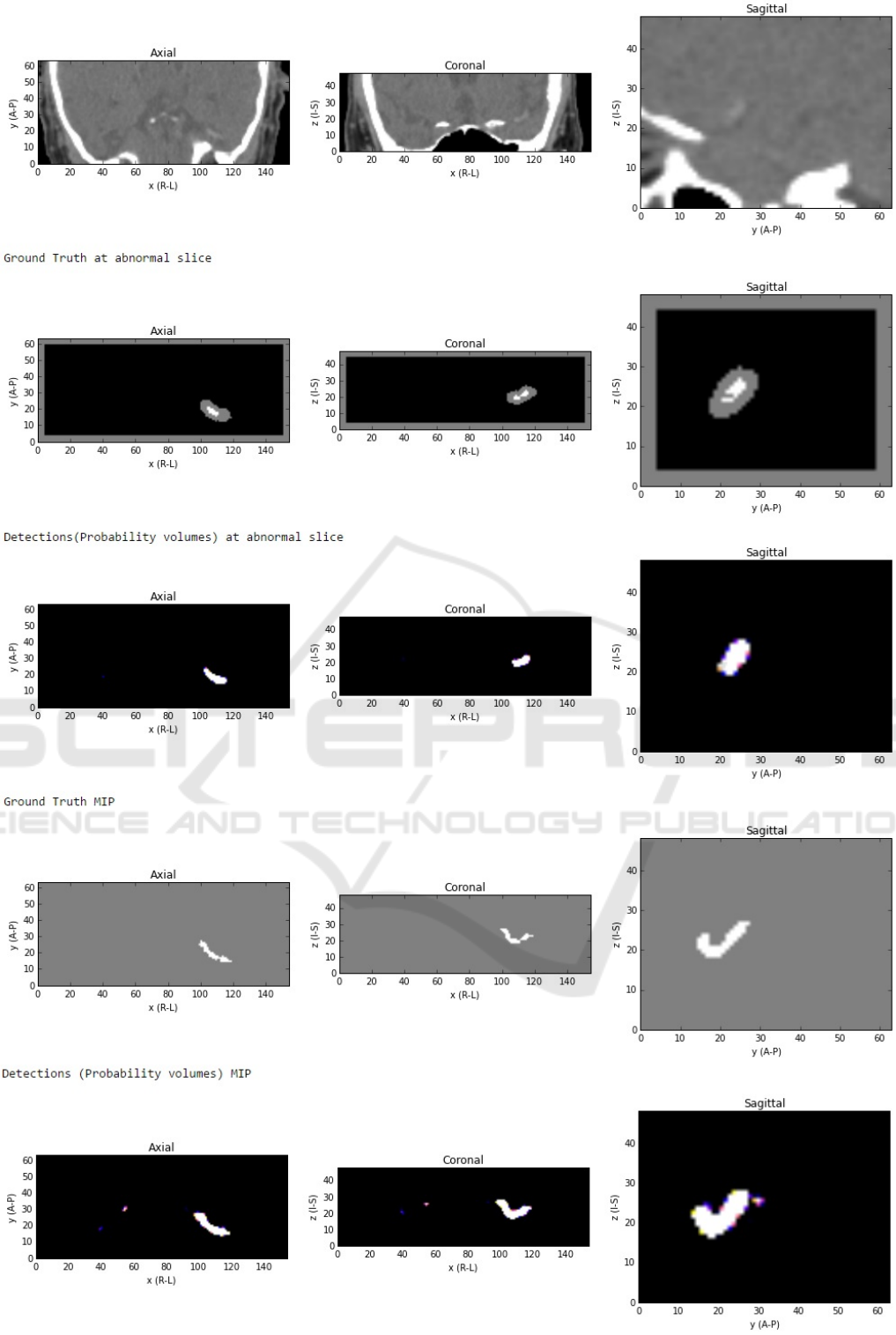

Figure 8: Top to bottom: CT image at the abnormal slice (** note posterior top, anterior bottom of the CT image) with thrombus clearly visible, ground truth segmentations at the abnormal slice (here:gray region is a ”do not care” zone), detection at the abnormal slice (clear detection), ground truth in a projection view through the whole volume, detection in a projection through the volume (a few false positive detections are present, but with lower certainty (dark blue and yellow colors as opposed to bright white true positive detections).

6 CONCLUSION

We have proposed a CNN for thrombus detection in brain CT. The suggested architecture utilises contralateral features and atlas information. The method is evaluated at the voxel level on 61 NCCT datasets and some example detection results are presented. Both quantitative and visual results are encouraging. Further investigation, as mentioned in the discussion, may lead to improvement of the detector to a level at which it could be applied in the clinical setting.

ACKNOWLEDGEMENTS

We wish to thank Alison O'Neil for her helpful comments on the manuscript draft.

REFERENCES

Anthimopoulos, M., Christodoulidis, S., Ebner, L., Christe, A., and Mougiakakou, S. (2016). Lung pattern classification for interstitial lung diseases using a deep convolutional neural network. *IEEE transactions on medical imaging*, 35(5):1207–1216.

Arevalo, J., Gonzalez, F. A., Ramos-Pollan, R., Oliveira, J. L., and Guevara Lopez, M. A. (2015). Convolutional neural networks for mammography mass lesion classification. In *Engineering in Medicine and Biology Society (EMBC), 2015 37th Annual International Conference of the IEEE*, pages 797–800. IEEE.

Bandyopadhyay, S. K. (2010). Breast asymmetry-tutorial review. *Breast*, 9(8).

Brosch, T., Yoo, Y., Tang, L. Y., Li, D. K., Traboulsee, A., and Tam, R. (2015). Deep convolutional encoder networks for multiple sclerosis lesion segmentation. In *Medical Image Computing and Computer-Assisted Intervention–MICCAI 2015*, pages 3–11. Springer.

Chawla, M., Sharma, S., Sivaswamy, J., and Kishore, L. (2009). A method for automatic detection and classification of stroke from brain ct images. In *Engineering in Medicine and Biology Society*, volume 2009, pages 3581–3584.

Ciresan, D., Giusti, A., Gambardella, L. M., and Schmidhuber, J. (2012). Deep neural networks segment neuronal membranes in electron microscopy images. In *Advances in neural information processing systems*, pages 2843–2851.

Ciresan, D. C., Giusti, A., Gambardella, L. M., and Schmidhuber, J. (2013). Mitosis detection in breast cancer histology images with deep neural networks. *Lecture Notes in Computer Science (including subseries Lecture Notes in Artificial Intelligence and Lecture Notes in Bioinformatics)*, 8150 LNCS(PART 2):411–418.

Dabbah, M. A., Murphy, S., Pello, H., Courbon, R., Beveridge, E., Wiseman, S., Wyeth, D., and Poole, I. (2014). Detection and location of 127 anatomical landmarks in diverse ct datasets. In *SPIE Medical Imaging*, pages 903415–903415. International Society for Optics and Photonics.

Davis, J. and Goadrich, M. (2006). The relationship between precision-recall and roc curves. In *Proceedings of the 23rd International Conference on Machine Learning*, ICML'06, pages 233–240.

Doyle, S., Vasseur, F., Dojat, M., and Forbes, F. (2013). Fully automatic brain tumor segmentation from multiple mr sequences using hidden markov fields and variational em. *Procs. NCI-MICCAI BraTS*, pages 18–22.

Dvorak, P. and Menze, B. (2015). Structured prediction with convolutional neural networks for multimodal brain tumor segmentation. *Proceedings of BRATS-MICCAI*.

Erihov, M., Alpert, S., Kisilev, P., and Hashoul, S. (2015). A cross saliency approach to asymmetry-based tumor detection. In *International Conference on Medical Image Computing and Computer-Assisted Intervention*, pages 636–643. Springer.

Gao, M., Xu, Z., Lu, L., Harrison, A. P., Summers, R. M., and Mollura, D. J. (2016). Multi-label deep regression and unordered pooling for holistic interstitial lung disease pattern detection. In *International Workshop on Machine Learning in Medical Imaging*, pages 147–155. Springer.

Geremia, E., Clatz, O., Menze, B. H., Konukoglu, E., Criminisi, A., and Ayache, N. (2011). Spatial decision forests for ms lesion segmentation in multi-channel magnetic resonance images. *NeuroImage*, 57(2):378–390.

Hasan, A., Meziane, F., and Khadim, M. (2016). Automated segmentation of tumours in mri brain scans. In *Proceedings of the 9th International Joint Conference on Biomedical Engineering Systems and Technologies (BIOSTEC 2016)*, pages 55–62. SCITEPRESS.

Havaei, M., Davy, A., Warde-Farley, D., Biard, A., Courville, A., Bengio, Y., Pal, C., Jodoin, P.-M., and Larochelle, H. (2016). Brain tumor segmentation with deep neural networks. *Medical Image Analysis*.

Huang, X., Cheripelli, B. K., Lloyd, S. M., Kalladka, D., Moreton, F. C., Siddiqui, A., Ford, I., and Muir, K. W. (2015). Alteplase versus tenecteplase for thrombolysis after ischaemic stroke (attest): a phase 2, randomised, open-label, blinded endpoint study. *The Lancet Neurology*, 14(4):368–376.

Kamnitsas, K., Chen, L., Ledig, C., Rueckert, D., and Glocker, B. (2015). Multi-scale 3D convolutional neural networks for lesion segmentation in brain MRI. *Ischemic Stroke Lesion Segmentation*, page 13.

Kamnitsas, K., Ledig, C., Newcombe, V. F., Simpson, J. P., Kane, A. D., Menon, D. K., Rueckert, D., and Glocker, B. (2016). Efficient multi-scale 3d cnn with fully connected crf for accurate brain lesion segmentation. *arXiv preprint arXiv:1603.05959*.

Ledig, C., Wolz, R., Aljabar, P., Lötjönen, J., Heckemann, R. A., Hammers, A., and Rueckert, D. (2012). Multi-class brain segmentation using atlas propagation and em-based refinement. In *2012 9th IEEE Inter-*

national Symposium on Biomedical Imaging (ISBI), pages 896–899. IEEE.

Li, Q., Cai, W., Wang, X., Zhou, Y., Feng, D. D., and Chen, M. (2014). Medical image classification with convolutional neural network. In *Control Automation Robotics & Vision (ICARCV), 2014 13th International Conference on*, pages 844–848. IEEE.

Li, W., Jia, F., and Hu, Q. (2015). Automatic segmentation of liver tumor in CT images with deep convolutional neural networks. *Journal of Computer and Communications*, 3(11):146.

Liswoska, A., Beveridge, E., and Poole, I. (2016). False positive reduction methods applied to dense vessel detection in brain ct images. Poster presented at Medical Imaging Summer School, Favigana, Italy.

O'Neil, A., Murphy, S., and Poole, I. (2015). Anatomical landmark detection in ct data by learned atlas location autocontext. In *MIUA*, pages 189–194.

Payan, A. and Montana, G. (2015). Predicting alzheimer's disease: a neuroimaging study with 3d convolutional neural networks. *arXiv preprint arXiv:1502.02506*.

Pereira, S., Pinto, A., Alves, V., and Silva, C. A. (2015). Deep convolutional neural networks for the segmentation of gliomas in multi-sequence mri. In *International Workshop on Brainlesion: Glioma, Multiple Sclerosis, Stroke and Traumatic Brain Injuries*, pages 131–143. Springer.

Prasoon, A., Petersen, K., Igel, C., Lauze, F., Dam, E., and Nielsen, M. (2013). Deep feature learning for knee cartilage segmentation using a triplanar convolutional neural network. In *Medical Image Computing and Computer-Assisted Intervention–MICCAI 2013*, pages 246–253. Springer.

Qiu, W., Yuan, J., Ukwatta, E., Sun, Y., Rajchl, M., and Fenster, A. (2013). Fast globally optimal segmentation of 3d prostate mri with axial symmetry prior. In *International Conference on Medical Image Computing and Computer-Assisted Intervention*, pages 198–205. Springer.

Rao, A., Ledig, C., Newcombe, V., Menon, D., and Rueckert, D. (2014). Contusion segmentation from subjects with traumatic brain injury: a random forest framework. In *2014 IEEE 11th International Symposium on Biomedical Imaging (ISBI)*, pages 333–336. IEEE.

Rao, V., Sarabi, M. S., and Jaiswal, A. (2015). Brain tumor segmentation with deep learning. *Proceedings of BRATS-MICCAI*.

Riedel, C. H., Zimmermann, P., Jensen-Kondering, U., Stingele, R., Deuschl, G., and Jansen, O. (2011). The importance of size successful recanalization by intravenous thrombolysis in acute anterior stroke depends on thrombus length. *Stroke*, 42(6):1775–1777.

Roth, H. R., Lu, L., Seff, A., Cherry, K. M., Hoffman, J., Wang, S., Liu, J., Turkbey, E., and Summers, R. M. (2014). A new 2.5 D representation for lymph node detection using random sets of deep convolutional neural network observations. In *Medical Image Computing and Computer-Assisted Intervention–MICCAI 2014*, pages 520–527. Springer.

Shin, H.-C., Roth, H. R., Gao, M., Lu, L., Xu, Z., Nogues, I., Yao, J., Mollura, D., and Summers, R. M. (2016). Deep convolutional neural networks for computer-aided detection: Cnn architectures, dataset characteristics and transfer learning. *IEEE transactions on medical imaging*, 35(5):1285–1298.

Urban, G., Bendszus, M., Hamprecht, F., and Kleesiek, J. (2014). Multi-modal brain tumor segmentation using deep convolutional neural networks. *Proceedings of BRATS-MICCAI*.

Wang, J., MacKenzie, J. D., Ramachandran, R., and Chen, D. Z. (2015). Neutrophils identification by deep learning and voronoi diagram of clusters. In *Medical Image Computing and Computer-Assisted Intervention–MICCAI 2015*, pages 226–233. Springer.

Wardlaw, J. M., Muir, K. W., Macleod, M.-J., Weir, C., McVerry, F., Carpenter, T., Shuler, K., Thomas, R., Acheampong, P., Dani, K., et al. (2013). Clinical relevance and practical implications of trials of perfusion and angiographic imaging in patients with acute ischaemic stroke: a multicentre cohort imaging study. *Journal of Neurology, Neurosurgery & Psychiatry*, pages jnnp–2012.

Wolterink, J. M., Leiner, T., Viergever, M. A., and Išgum, I. (2015). Automatic coronary calcium scoring in cardiac CT angiography using convolutional neural networks. In *Medical Image Computing and Computer-Assisted Intervention–MICCAI 2015*, pages 589–596. Springer.

Yang, D., Zhang, S., Yan, Z., Tan, C., Li, K., and Metaxas, D. (2015). Automated anatomical landmark detection on distal femur surface using convolutional neural network. In *Biomedical Imaging (ISBI), 2015 IEEE 12th International Symposium on*, pages 17–21. IEEE.

Zhao, L., Wu, W., and Corso, J. J. (2013). Semi-automatic brain tumor segmentation by constrained mrfs using structural trajectories. In *International Conference on Medical Image Computing and Computer-Assisted Intervention*, pages 567–575. Springer.

Zikic, D., Glocker, B., Konukoglu, E., Criminisi, A., Demiralp, C., Shotton, J., Thomas, O., Das, T., Jena, R., and Price, S. (2012). Decision forests for tissue-specific segmentation of high-grade gliomas in multi-channel mr. In *International Conference on Medical Image Computing and Computer-Assisted Intervention*, pages 369–376. Springer.